

Thermonuclear Type-I X-ray Bursts and Burst Oscillations from the Eclipsing AMXP Swift J1749.4–2807

A. C. Albayati,^{1*} P. Bult,^{2,3} D. Altamirano,¹ J. Chenevez,⁴ S. Guillot,⁵
 T. Güver,^{6,7} G. K. Jaisawal,⁴ C. Malacaria,⁸ G. C. Mancuso,^{9,10} A. Marino,^{11,12,13}
 M. Ng,¹⁴ A. Sanna,¹⁵ T. E. Strohmayer³

¹*School of Physics and Astronomy, University of Southampton, Southampton, SO17 1BJ, UK*

²*Department of Astronomy, University of Maryland, College Park, MD 20742, USA*

³*Astrophysics Science Division, NASA Goddard Space Flight Center, Greenbelt, MD 20771, USA*

⁴*DTU Space, Technical University of Denmark, Elektrovej 327-328, Lyngby DK-2800, Denmark*

⁵*Institut de Recherche en Astrophysique et Planétologie, UPS-OMP, CNRS, CNES, 9 avenue du Colonel Roche, BP 44346, F-31028 Toulouse Cedex 4, France*

⁶*Istanbul University, Science Faculty, Department of Astronomy and Space Sciences, Beyazit, 34119, İstanbul, Turkey*

⁷*Istanbul University Observatory Research and Application Center, Istanbul University 34119, İstanbul Turkey*

⁸*International Space Science Institute (ISSI), Hallerstrasse 6, 3012 Bern, Switzerland*

⁹*Instituto Argentino de Radioastronomía (CCT-La Plata, CONICET; CICPBA), C.C. No. 5, 1894 Villa Elisa, Argentina*

¹⁰*Facultad de Ciencias Astronómicas y Geofísicas, Universidad Nacional de La Plata, Paseo del Bosque s/n, 1900 La Plata, Argentina*

¹¹*Institute of Space Sciences (ICE, CSIC), Campus UAB, Carrer de Can Magrans s/n, E-08193 Barcelona, Spain*

¹²*Institut d'Estudis Espacials de Catalunya (IEEC), Carrer Gran Capità 2–4, E-08034 Barcelona, Spain*

¹³*INAF, Istituto di Astrofisica Spaziale e Fisica Cosmica, Via U. La Malfa 153, I-90146 Palermo, Italy*

¹⁴*MIT Kavli Institute for Astrophysics and Space Research, Massachusetts Institute of Technology, 77 Massachusetts Avenue, Cambridge, MA 02139, USA*

¹⁵*Dipartimento di Fisica, Universit 'a degli Studi di Cagliari, SP Monserrato-Sestu km 0.7, Monserrato 09042, Italy*

Accepted XXX. Received YYY; in original form ZZZ

ABSTRACT

Swift J1749.4-2807 is the only known eclipsing accreting millisecond X-ray pulsar. In this paper, we report on 7 thermonuclear (Type-I) X-ray bursts observed by *NICER* during its 2021 outburst. The first 6 bursts show slow rises and long decays, indicative of mixed H/He fuel, whereas the last burst shows fast rise and decay, suggesting He-rich fuel. Time-resolved spectroscopy of the bursts revealed typical phenomenology (i.e., an increase in black body temperature during the burst rise, and steady decrease in the decay), however they required a variable N_{H} . We found that the values of N_{H} during the bursts were roughly double those found in the fits of the persistent emission prior to each burst. We interpret this change in absorption as evidence of burst-disc interaction, which we observe due to the high inclination of the system. We searched for burst oscillations during each burst and detected a signal in the first burst at the known spin frequency of the neutron star (517.92 Hz). This is the first time burst oscillations have been detected from Swift J1749.4-2807. We further find that each X-ray burst occurs on top of an elevated persistent count rate. We performed time-resolved spectroscopy on the combined data of the bursts with sufficient statistics (i.e., the clearest examples of this phenomenon) and found that the black body parameters evolve to hotter temperatures closer to the onset of the bursts. We interpret this as a consequence of an unusual marginally stable burning process similar to that seen through mHz QPOs.

Key words: stars: neutron – stars: individual (Swift J1749.4–2807) – X-rays: binaries – X-rays: bursts

1 INTRODUCTION

In a low-mass X-ray binary (LMXB) a neutron star or a black hole primary accretes matter from a stellar mass companion star via Roche lobe overflow. This material generates a vast amount of X-rays as it releases gravitational potential energy in the accretion disc around the primary (see, e.g., [Tauris & van den Heuvel 2006](#), for a review). In the case of neutron star LMXBs matter is accreted onto the neutron star where it spreads across the surface and is compressed by the intense gravity. When the matter reaches a critical density, it ignites in a run-away thermonuclear explosion – a Type-I X-ray burst (hereafter simply “X-ray burst” or “burst”). X-ray bursts appear as a sudden increase in X-ray emission over timescales of seconds, where the burst rises are typically $\lesssim 1 - 10$ s, followed by a roughly exponential decay over tens to hundreds of seconds (e.g., [Galloway et al. 2008](#)). Spectral fitting of X-ray bursts has revealed peak black body temperatures of $1 - 3$ keV (e.g., [MINBAR¹](#), [Galloway et al. 2020](#)), and the ignited material can have a pure or mixed composition of hydrogen, helium, and sometimes carbon (see, e.g., [Lewin et al. 1993](#); [Strohmayer & Bildsten 2006](#), for reviews). X-ray photons released by an X-ray burst can interact with the accretion disc, leading to changes in the disc structure, mass outflows from the disc, and a drag being exerted on the disc (e.g., [Degenaar et al. 2016, 2018](#), and references therein).

Swift J1749.4–2807 (hereafter Swift J1749) was discovered in 2006 through observations made with the Neil Gehrels Swift Observatory (*Swift*; [Gehrels 2004](#)) Burst Alert Telescope (BAT; [Krimm et al. 2013](#)) as a burst-only source (GRB060602B; [Schady et al. 2006](#); [Beardmore et al. 2006](#)). Evidence from the soft spectra suggested that it might have been an X-ray burst rather than a classical gamma-ray burst ([Palmer et al. 2006](#)). The burst origin was confirmed to be from an accreting neutron star in 2009 when another outburst from the source was observed with *Swift*/BAT, *Swift* X-Ray Telescope (XRT; [Burrows et al. 2003](#)), and *XMM-Newton*’s European Photon Imaging Camera (EPIC; [Strüder et al. 2001](#)). The detection of an X-ray burst lasting ~ 10 s was reported during the 2009 outburst, and an approximate bolometric flux of $7_{-2}^{+4} \times 10^{-8} \text{ erg s}^{-1} \text{ cm}^{-2}$ was estimated ([Wijnands et al. 2009](#)). The detection of this X-ray burst allowed for an upper limit estimation on the distance to the source of 6.7 ± 1.3 kpc. A persistent X-ray counterpart was found with the *Swift*/XRT data, and supported by archival *XMM-Newton* data showing a constant faint point source with coordinates consistent with the *Swift*/XRT findings ([Halpern 2006](#); [Wijnands et al. 2009](#)).

Swift J1749 was detected again in 2010 by the *INTEGRAL* Joint European X-Ray Monitor (JEM-X2; [Lund et al. 2003](#)) and observed further by *Swift* ([Pavan et al. 2010](#)), and the Rossi X-ray Timing Explorer (*RXTE*; [Jahoda et al. 2006](#)). The observations from *RXTE* revealed that Swift J1749 is an accreting millisecond X-ray pulsar (AMXP, see [Di Salvo & Sanna 2022](#); [Patruino & Watts 2021](#), for reviews), detecting strong coherent pulsations at 517.9 Hz and at its first over-tone (1035.8 Hz; [Altamirano et al. 2010, 2011](#); [Bozzo et al. 2010](#)). The orbital period is 8.82 hrs, suggesting a minimum companion mass of $0.475 M_{\odot}$ ([Belloni](#)

Table 1. Details of the *NICER* Observation IDs analysed in this paper. Quoted exposure times are as after processing. Only the last digit (x) of ObsIDs are listed, where ObsID = 465801010x. Times are listed in Terrestrial Time.

ObsID x	Start Time (MJD)	Date (DD-MM-YY)	Exposure (sec)	X-ray Bursts
1	59274.61971	01-03-21	9272	-
2	59275.00551	02-03-21	18150	Yes
3	59276.03994	03-03-21	9783	Yes
4	59277.01551	04-03-21	11637	Yes
5	59278.04650	05-03-21	16957	Yes
6	59281.20661	08-03-21	5263	-
7	59282.04564	09-03-21	11283	Yes
8	59283.01358	10-03-21	12035	-

et al. 2010; [Strohmayer & Markwardt 2010](#)). The *RXTE* observations also revealed that the system was eclipsing ([Markwardt & Strohmayer 2010](#)), making it the first (and so far, only) detected eclipsing AMXP, allowing for the inclination of the system to be constrained to $i \approx 74^{\circ} - 77^{\circ}$ ([Altamirano et al. 2011](#)). During the 2010 outburst, the second X-ray burst from Swift J1749 was detected ([Chenevez et al. 2010](#); [Ferrigno et al. 2011](#)), however statistics from the *INTEGRAL*/JEM-X2 data were not sufficient to perform detailed spectral analysis.

After over 10 years in quiescence, a new outburst of Swift J1749 was detected by *INTEGRAL*/JEM-X during Galactic bulge monitoring observations carried out on 28 February - 1 March 2021 ([Mereminskiy et al. 2021](#)). *NICER* turned to the source on 1 March (MJD 59274) and observed regularly for the duration of the outburst ([Bult et al. 2021b](#)). In this paper we report on the detection of 7 X-ray bursts with *NICER*, and their detailed analysis. The detailed pulsar timing analysis of the full outburst has been presented in [Sanna et al. \(2022\)](#), and analysis of the outflows and spectral evolution of this outburst has been presented in [Marino et al. \(2022\)](#).

2 OBSERVATIONS

NICER observed Swift J1749 between 1 March and 1 May 2021, generating a total of 33 Observation IDs (ObsIDs 4658010101 – 4658010133). We identified the section of the outburst containing X-ray bursts and selected 8 ObsIDs encompassing this section of the outburst to analyse in detail (see [Sanna et al. 2022](#); [Marino et al. 2022](#), for analysis on a wider range of ObsIDs from this outburst). These ObsIDs, each containing several data segments (or “pointings”)², are listed in Table 1. To process the data, we used HEASOFT v6.28 ([HEASARC 2014](#)) and NICERDAS v7 with standard filtering criteria. The total good exposure after processing was 94.4 ksec.

² After filtering, the 8 ObsIDs we analysed each contain between 6 – 16 pointings, typically lasting $\sim 1000 - 2000$ s.

¹ <https://burst.sci.monash.edu/minbar>

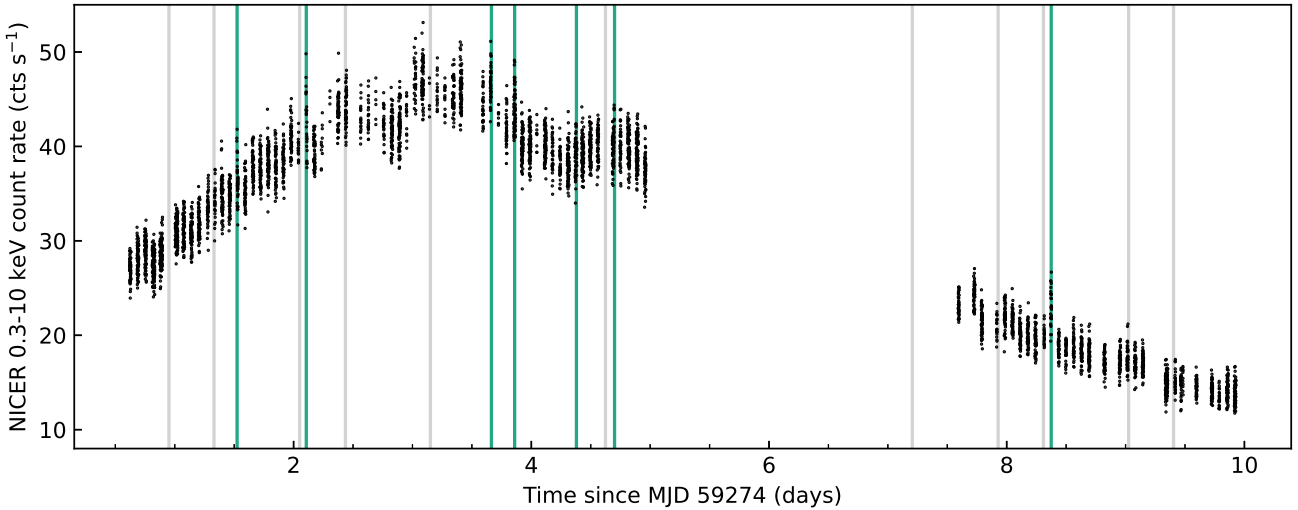


Figure 1. *NICER* long-term light curve of the section of Swift J1749’s 2021 outburst which contains Type-I X-ray bursts with 16 s time resolution in the 0.3 – 10 keV energy band. The outburst contains 7 thermonuclear X-ray bursts detected in March 2021, denoted by teal lines. 11 eclipses were also detected during this time, and are denoted by grey lines (note that there was a small section of eclipse-only data at ~ 7.2 days).

3 DATA ANALYSIS AND RESULTS

3.1 Outburst Evolution and Occurrence of X-ray Bursts

The outburst evolution of Swift J1749 between 1 – 10 March 2021 (MJD 59274-59283), including X-ray bursts and eclipses, is shown in Figure 1. We constructed a 0.3 – 10 keV long-term light curve using 16 s bins. We searched for X-ray bursts and found 7 in total across 5 ObsIDs (see Table 1). In this paper, we do not analyse the full outburst as observed by *NICER*, but only the ObsIDs where X-ray bursts were observed.

From MJD 59274.61971 ($t = 0.6$ days in Figure 1, with reference time MJD 59274) the light curve shows the persistent count rate to rise from ~ 28 cts s^{-1} to ~ 36 cts s^{-1} over one day, at which point we detected the first X-ray burst (MJD 59275.52449). The second observed X-ray burst occurred half a day later (MJD 59276.10658) at a persistent rate of ~ 42 cts s^{-1} . The persistent count rate peaked at approximately 50 cts s^{-1} at $t \approx 3.0$ days, and began to drop until the beginning of a large visibility gap at $t \approx 5.0$ days where it reached ~ 37 cts s^{-1} . During this time, *NICER* observed 4 more X-ray bursts (at MJD 59277.66427, 59277.85985, 59278.37967, 59278.70041) and 6 eclipses in total. Observations resumed at $t \approx 7.2$ days during an eclipse, where the persistent count rate was at ~ 24 cts s^{-1} following this eclipse. We saw two more eclipses as the persistent count rate decreased further to roughly 20 cts s^{-1} at $t \approx 8.3$ days, where a bright X-ray burst occurred (MJD 59282.37445). After the final X-ray burst observed by *NICER* the persistent count rate continued to decrease.

Inspection of the pointings containing X-ray bursts revealed that the count rate appears to increase before the onset of each X-ray burst by $\sim 20\%$. We hereafter refer to this enhanced emission immediately prior to each X-ray burst as “pre-burst emission”.

3.2 X-ray Bursts

3.2.1 Light Curves

We extracted individual X-ray burst light curves in the 0.3 – 10 keV energy band using 1 s bins (Figure 2). We will refer to individual X-ray bursts as B1, B2, ... and B7 for the first, second, ... and seventh bursts respectively.

In order to define the burst start and end times, first we identified the peak of the burst as the 1 s bin with the highest count rate. We defined the start of each X-ray burst by searching backwards in time from the peak bin, and identifying the first time bin in which the count rate drops below 10% of the peak. The burst rise time (t_{rise}) was defined as the time between the start and peak of the X-ray burst. We found the end of each X-ray burst by taking the median of 10 s data segments from the burst peak, and searching forward in time for the first segment to fall below 10% of the peak count rate. We defined the burst end to be the start time of this segment. The decay time (t_{decay}) is defined as the time between the peak and the end of the X-ray burst.

When considering the persistent count rate with regards to the background rate outside of the X-ray burst, in order to differentiate it from how we define persistent emission in our spectral analysis, we will hereafter refer to the persistent count rate as the “continuum count rate”. We found the continuum count rate by taking the median count rate of the data from the beginning of the pointing including an X-ray burst until 30 s before the burst peak. There was no data collected due to a drop in telemetry during the rise of B3, so we manually adjusted the start time such that the tail of the burst was aligned with the other bursts, and calculated the continuum count rate by taking the median of the first 500 s of data from the pointing containing the burst. For this reason, B3 is excluded from spectral analysis.

We find that the first 6 X-ray bursts in this outburst from Swift J1749 are all similar in profile, with an average

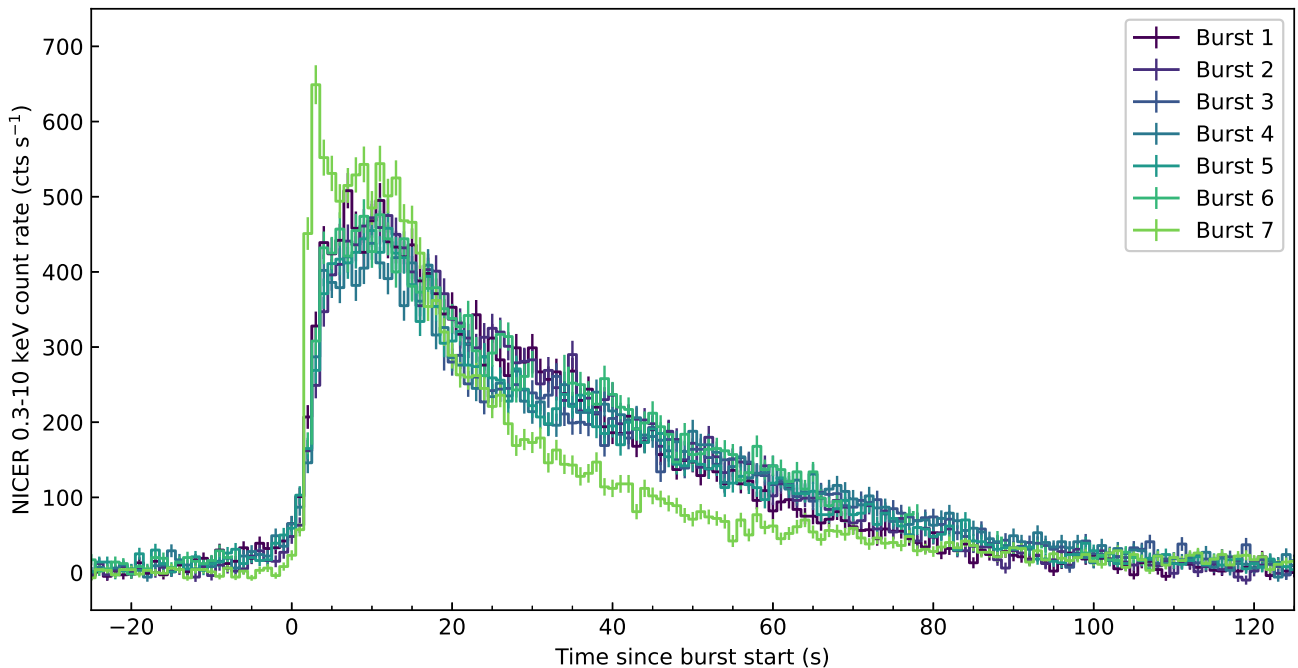


Figure 2. Background-subtracted light curves of the 7 X-ray bursts from Swift J1749 aligned by burst onset (with manual optimisation for alignment in this figure) with 1 s time resolution in the 0.3 – 10 keV energy band. The rise of B3 was not observed, so manual adjustments were made to optimise tail alignment.

rise time (excluding B3) of 9.7 s ($\sigma = 3.9$ s for the distribution of burst rise times, Figure 2). This is longer than previously reported X-ray bursts from this source³. With a rise time of 2 s, a more rapid decay and a higher peak count rate than the first 6 bursts, B7 more closely resembles the profiles of historic X-ray bursts from this source (see, Ferrigno et al. 2011). From these rise times, we can infer that the composition is likely H-rich fuel in the case of B1 – 6, and comparatively He-rich for B7 (Galloway et al. 2008).

Recent observations of X-ray bursts from SAX J1808.4–3658 and MAXI J1807+132 with *NICER* data have revealed short plateaus, or “pauses”, in their rises (Bult et al. 2019; Albayati et al. 2021). We looked at the 0.1 s binned light curves to check for these, but found none.

3.2.2 Persistent Emission

To fit the persistent emission, we took the pointing immediately before the one containing each X-ray burst, or the one before that if the one immediately before the X-ray burst was eclipsed⁴. This pointing used for the persistent emission was within the same observation in all cases. Background and total spectra were created using `nibackgen3C50` (Remillard

et al. 2022), and the total spectra were rebinned using the optimal binning scheme of Kaastra & Bleeker (2016) with the additional requirement that each spectral bin contains at least 50 photons. In the case of B1, B2, B4, B5, and B7, we fitted the 1 – 9 keV (chosen due to background noise dominating outside this range) energy spectrum using the `Xspec` v.12.11.1 (Arnaud 1996) model

$$\text{tbabs} \times \text{powerlaw},$$

setting the photoelectric cross-sections and the element abundances to the values provided by Verner et al. (1996) and Wilms et al. (2000) respectively. We initially included a disc black body component, however we found that this component was not significant in all cases, so it was omitted. For all spectrally analysed X-ray bursts, we found an average column density of $N_{\text{H}} = (3.52 \pm 0.03) \times 10^{22} \text{ cm}^{-2}$ which broadly agrees with values in literature (e.g. Ferrigno et al. 2011; Bult et al. 2021b; Marino et al. 2022).

The photon indices, absorbed 0.5 – 10 keV fluxes (following Marino et al. 2022), and reduced χ^2 obtained from modelling the persistent emissions are reported in Table 2. The errors are quoted at a 90% confidence interval.

3.2.3 Time-Resolved Spectroscopy of X-ray Bursts

We used a 0.1 s binned 1 – 9 keV light curve of each X-ray burst (using the previously calculated start and end times) to generate GTIs that set the temporal boundaries for the bins that we use for time-resolved spectroscopy (TRS). We combined 0.1 s light curve bins until we had a time interval containing at least 1000 counts. The last bin was discarded

³ We note that these bursts were detected by instruments with different energy bands and sensitivities to *NICER*, Wijmands et al. (2009) detected by *Swift*/BAT (>10 keV) and Ferrigno et al. (2011) by *INTEGRAL*/JEM-X2 (3 – 20 keV).

⁴ This decision was made as our tests had shown that the data immediately prior to the X-ray bursts, including the raised pre-burst emission, spectrally evolve.

Table 2. The photon indices, absorbed 0.5 – 10 keV fluxes, and reduced χ^2 obtained from modelling the persistent emissions of Swift J1749, with all errors quoted at a 90% confidence interval.

Burst	N_{H} (10^{22} cm^{-2})	Photon Index	Absorbed Flux ($10^{-10} \text{ erg cm}^{-2} \text{ s}^{-1}$)	χ^2_{ν} (χ^2/dof)
1	3.59 ± 0.08	2.36 ± 0.05	2.56 ± 0.02	215/162
2	3.62 ± 0.08	2.36 ± 0.05	3.10 ± 0.03	196/159
4	3.63 ± 0.09	2.50 ± 0.06	3.05 ± 0.03	134/144
5	3.53 ± 0.06	2.43 ± 0.04	2.82 ± 0.02	238/167
6	3.55 ± 0.07	2.44 ± 0.04	2.99 ± 0.02	141/163
7	3.11 ± 0.09	2.19 ± 0.06	1.49 ± 0.02	164/138

as it usually had insufficient counts for spectral fitting. Individual spectra were extracted for each TRS bin, and were rebinned using optimal binning to a minimum of 25 counts per energy bin. A single background spectrum was extracted over the whole X-ray burst using `nibackgen3C50` and was used in fitting each spectra in the X-ray burst.

We fitted each TRS spectrum in the 1 – 9 keV energy band with the `Xspec` model

$$\text{tbabs} \times (\text{bbodyrad} + \text{powerlaw})$$

allowing `tbabs` and `bbodyrad` to vary, with the powerlaw component fixed to the best fit parameters from the persistent emission fits (see Table 2). We found the unabsorbed bolometric flux by fitting with `cflux` in the 0.001–100 keV band on `bbodyrad`. Errors were found using `Xspec`'s `chain` utility and are quoted for a 90% confidence interval.

We chose to allow the absorption to vary as using a fixed- N_{H} black body method (with N_{H} fixed to the values found in the persistent emission, Table 2) in most cases resulted in high reduced χ^2 values, and implementing the f_a -method (Worpel et al. 2013, 2015) to scale the persistent emission did not improve the fits⁵. We did, however, find that the fit could be improved by accounting for varying absorption throughout the burst. In order to confirm that varying absorption produced the best fits, we also varied the powerlaw photon index, however this produced unphysically high photon indices. We provide a more detailed discussion and comparison of fits in Appendix A.

In Figure 3 we show the best-fit parameters for the time-resolved spectroscopy of B1, B2, B4, and B7 as examples of our results. The bolometric unabsorbed fluxes (F_{bol}) and black body temperatures (kT_{bb}) of all spectrally analysed bursts approximately follow the light curve contours, increasing during the burst rise and decreasing during the decay. This is expected for X-ray bursts (see, e.g., Lewin et al. 1993, for a review). The peak fluxes are reported in Table 3. In Table 3, we also report the X-ray burst fluences and time scales τ ($= \text{fluence} / \text{peak } F_{\text{bol}}$), where the fluences were calculated over the burst duration (i.e., $t_{\text{rise}} + t_{\text{decay}}$).

We found that the values of N_{H} during the X-ray bursts were higher by an average of $(1.98 \pm 0.08) \times 10^{22} \text{ cm}^{-2}$ than those found in the fits of the persistent emission. From Figure 3, we can see that there was no clear evolution of N_{H} in any of the bursts, however they appear to be correlated

with black body normalisation. This is likely due to poor statistics.

We note that none of these bursts exhibit photospheric radius expansion (PRE; see, e.g., Galloway et al. 2008, for a review) characterised by an increase in black body normalisation and decrease in kT_{bb} at the burst peak. The brightest X-ray burst in our data set (B7) is not as bright as those seen in historic data, therefore a new upper limit on distance is not possible to attain.

3.3 Raised Pre-Burst Emission

3.3.1 Light Curves of Pre-Burst Emission

To investigate the enhanced pre-burst emission in the X-ray burst light curves, we defined a ‘‘baseline’’ count rate for each X-ray burst by taking the mean count rates of the pointings immediately before and after the pointing containing the X-ray burst, and taking an average of these two values. Baseline-subtracted light curves of each X-ray burst are shown in Figure 4. The count rate before and after the bursts appear to be elevated compared with neighbor pointings.

In the case of B1, B2, B4, B5, and B6 the pre-burst count rate increases by $\sim 8 \text{ cts s}^{-1}$ before the burst onset. B7's pre-burst count rate also increases to $\sim 8 \text{ cts s}^{-1}$, but it dips back down to the baseline count rate $\sim 40 \text{ s}$ before the X-ray burst onset. In the light curves where we have sufficient data (B4-7), we can see that these phenomena occur from $\sim 200\text{-}250 \text{ s}$ before the burst onset.

3.3.2 Time-Resolved Spectroscopy of Pre-Burst Emission

To investigate the spectral evolution of the emission leading up to the X-ray bursts, we considered the best examples of X-ray bursts with raised pre-burst count rate (B4, B5, and B6) and performed time-resolved spectroscopy.

We isolated 4 bins of data each 50 s in length leading up to 10 s before the start of the X-ray burst (see Figure 5). We extracted event files that combined all bin 1 segments, all bin 2 segments, etc., and the same for the persistent emission (data selection for persistent spectra defined in §3.2.2). We justify combining the data in this way by noting that the persistent emission spectral shapes are consistent within errors, suggesting that all three observations sample the same source state.

We extracted background and total spectra in the 1–9 keV energy band for each bin and the persistent emission using `nibackgen3C50`, and re-binned the total spectra using optimal binning to a minimum of 50 cts per energy bin. While investigating the combined persistent emission spectrum, we found an absorption line at $\sim 7 \text{ keV}$ which we fitted with a Gaussian. This absorption line was also found by Marino et al. (2022) who identified it as a slightly blueshifted Fe XXVI absorption line commonly found in high-inclination LMXBs (see, e.g., Ponti et al. 2014).

We simultaneously fit all the bins and persistent spectra with the spectral model stated in §3.2.2, including a Gaussian component to account for the absorption line found in the persistent spectrum. For these fits, we estimate the confidence regions using MCMC contours. Firstly, we fit the data allowing both the black body and power law parameters to vary freely, whilst the N_{H} parameters were tied. The black

⁵ We note that allowing N_{H} to vary also improved the fits when we used the data immediately prior to the burst (including the raised pre-burst emission) as our background spectra.

Table 3. Overview of X-ray burst information and parameters calculated from time-resolved spectroscopy (left to right): burst number, Observation ID where only the last digit (x) of ObsIDs are listed (ObsID = 465801010x), the peak unabsorbed bolometric flux, total bolometric burst fluence, burst rise time, burst decay time, characteristic timescale, and average hydrogen column density.

#	ObsID	Onset Time (MJD)	Peak F_{bol} ($10^{-9} \text{ erg s}^{-1} \text{ cm}^{-2}$)	Fluence ($10^{-7} \text{ erg cm}^{-2}$)	t_{rise} (s)	t_{decay} (s)	τ (s)	Average N_{H} (10^{22} cm^{-2})
1	2	59275.52449	$15.85^{+3.91}_{-2.91}$	3.62 ± 0.13	8	65	22.84 ± 4.08	5.63 ± 0.17
2	3	59276.10658	$14.40^{+3.27}_{-2.43}$	3.71 ± 0.13	13	65	25.79 ± 4.19	5.51 ± 0.16
4	4	59277.85985	$14.96^{+4.41}_{-3.05}$	3.55 ± 0.13	11	75	23.70 ± 5.03	5.52 ± 0.14
5	5	59278.37967	$12.62^{+2.79}_{-2.13}$	3.36 ± 0.12	14	67	26.66 ± 4.21	5.60 ± 0.17
6	5	59278.70041	$13.21^{+2.76}_{-2.11}$	3.49 ± 0.13	10	58	26.43 ± 3.90	5.46 ± 0.17
7	7	59282.37445	$49.12^{+20.36}_{-14.06}$	3.84 ± 0.35	2	50	7.81 ± 2.02	5.33 ± 0.24

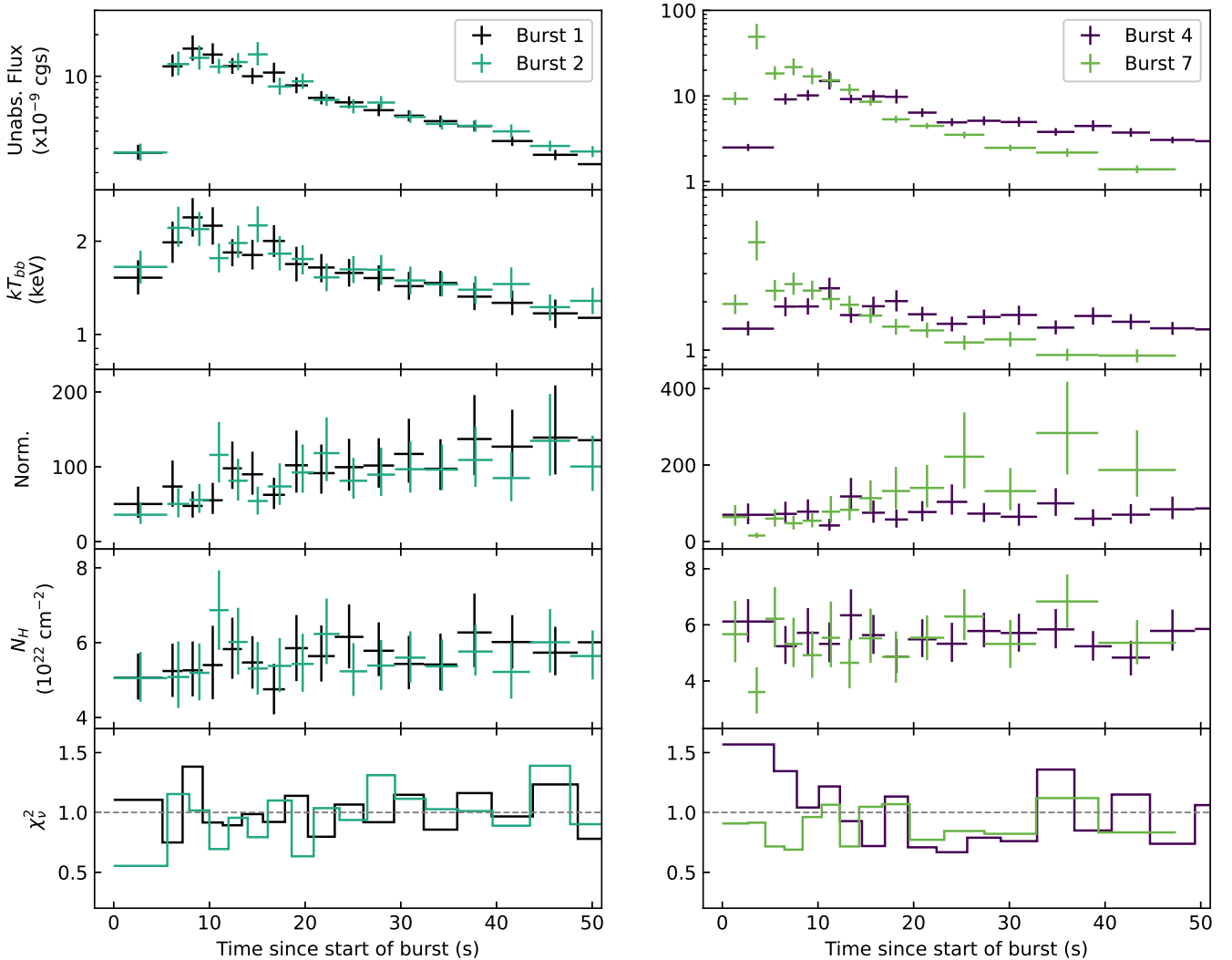


Figure 3. Time-resolved spectroscopy of bursts 1 and 2 (left), and 4 and 7 (right) using a variable N_{H} method. From top, we show the unabsorbed bolometric flux (in units of $\text{erg s}^{-1} \text{ cm}^{-2}$), the black body temperature and normalisation, the variable Hydrogen column density and the reduced χ^2 . Note the log scaling in the first two rows.

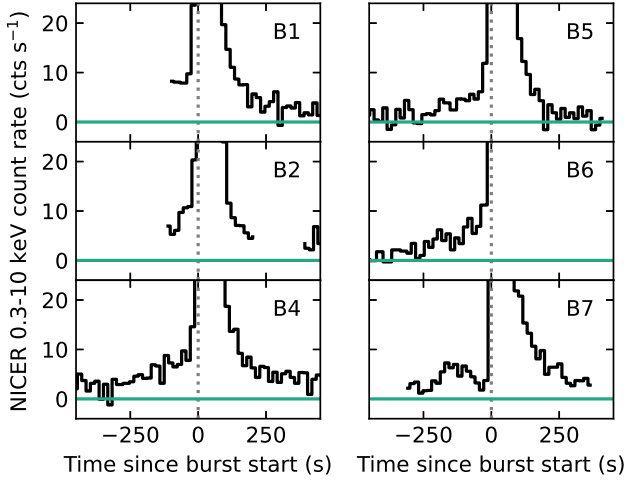


Figure 4. Baseline count rate subtracted light curves of the X-ray bursts (excluding B3) from Swift J1749 with 16 s time resolution in the 0.3 – 10 keV energy band. The burst start times are marked by vertical dotted lines. Error bars omitted for clarity, but are typically ± 1 cts s^{-1} .

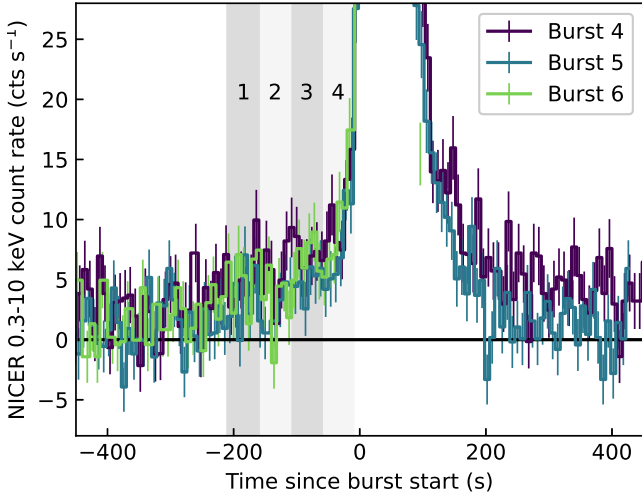


Figure 5. Baseline emission subtracted light curves of B4, B5, and B6 from Swift J1749 with 8 s time resolution in the 0.3 – 10 keV energy band. The 4 bins of 50 s duration each used in the spectral analysis of the pre-burst rising persistent count rate are denoted by grey bands.

body temperature evolved to hotter temperatures compared with the persistent spectrum, whilst the power law parameters remained consistent with the persistent fits. In order to better constrain the black body parameters, we performed fits where the power law parameters were tied together for all the bins including the persistent spectrum, and only the black body parameters were allowed to vary freely. We show the MCMC contours from this fit in Figure 6. Compared with the persistent spectrum, the black body temperature (kT_{bb}) evolves towards hotter temperatures closer to the burst onset, whilst the normalisation decreases. We calcu-

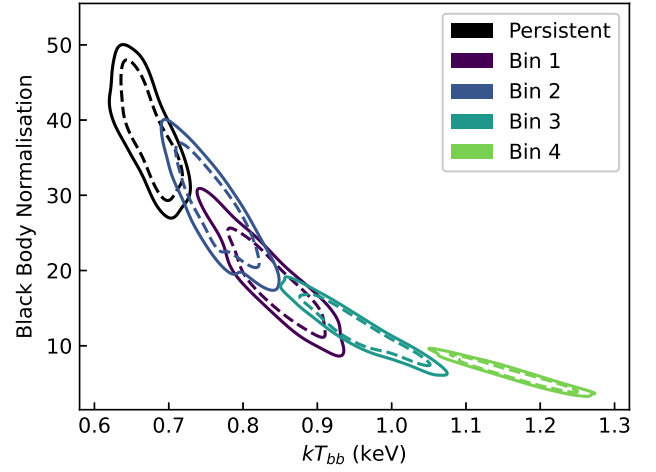


Figure 6. A contour plot created using MCMC, showing the black body parameter evolution from fitting the pre-burst emission with the model $tbabs \times (diskbb + powerlaw)$, where *only* `diskbb` was allowed to vary freely. Confidence levels are shown at 68% (dotted line) and 90% (solid line).

lated the absorbed flux for each bin including the persistent bin, and found that it increases closer to the burst onset.

3.4 Search for Burst Oscillations

We searched all 7 X-ray bursts for the presence of burst oscillations using a Z_2^2 -based search method (Buccheri et al. 1983). First we corrected the event times to the solar system barycentre using the DE-430 ephemeris (Folkner et al. 2014) and the source coordinates reported by Jonker et al. (2013). Next, we used the binary ephemeris reported by Sanna et al. (2022) to correct the event times for the Doppler shift introduced by the orbital motion of the neutron star. For a given X-ray burst, we then used all events in the 0.5 – 10 keV energy range within a 100 s time interval starting at the burst onset. We then used a sliding window method to extract a series of views on the data, where we used window durations of $T = 4, 8,$ and 16 s with steps of $T/4$. For each extracted window, we evaluated the Z_2^2 score on a grid of frequencies, defined as a 4 times oversampled Fourier frequency grid that was centred on the 518 Hz neutron star spin frequency and has a width of 10 Hz. If we assume that Poisson counting statistics hold, then the Z_2^2 scores in absence of a signal should follow a χ^2 distribution with four degrees of freedom. Hence, if a measured Z_2^2 score exceeded the trial-adjusted 3σ detection threshold set by this distribution, then we adopted it as a burst oscillation candidate.

A single candidate burst oscillation was found in B1, making it the first burst oscillation candidate found in an X-ray burst from Swift J1749. The candidate had a frequency of 517.92 Hz, which is entirely consistent with the known spin frequency of the neutron star (Sanna et al. 2022). This candidate was found in both 8 s and 16 s duration windows, with peak scores of 33 and 40, respectively. In both cases the highest score was found when the window position was centred on $t = 8$ s, (relative to the onset time, see the top panel of Figure 7), meaning that the burst oscillation candidate was found at the peak intensity of the X-ray burst. In or-

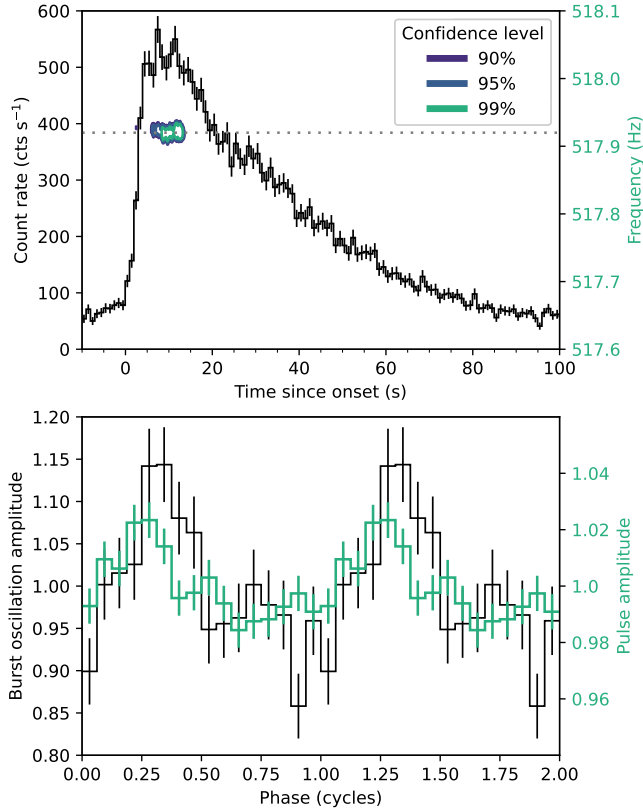


Figure 7. Burst oscillation detection in Burst 1. The top panel shows the X-ray burst light curve at 0.5 s time resolution (left axis) along with a dynamic power spectrum calculated using a 16 s duration sliding window (contours, right axis). The dotted line indicates the known 517.92 Hz pulsar spin frequency. The bottom panel shows two cycles of the burst oscillation waveform (black) compared to the contemporaneous coherent pulsation in the non-burst emission (teal, Sanna et al. 2022). Because the coherent pulsation has a much smaller amplitude, we plotted this second waveform against the zoomed-in scale of the left axis.

der to verify the detection significance of this candidate, we used a Monte Carlo approach to simulate the true noise distribution of the search method (Bilous & Watts 2019; Bult et al. 2021a). Compared to this simulated distribution, we find that the measured signal had a detection significance of 3.7σ .

Taking the epoch during which the burst oscillation is detected ($t = 2 - 22$ s after onset), we folded the data on the burst oscillation frequency to obtain its waveform (Figure 7, bottom panel). This waveform is somewhat asymmetric and has a fractional root mean square (rms) amplitude of $(7.1 \pm 1.5)\%$. In an attempt to investigate the energy dependence of the burst oscillation amplitude, we subdivided the energy range into three bands (0.5 – 2, 2 – 4, 4 – 10 keV), and constructed the burst oscillation waveform in each band. The oscillation was significantly detected in each band, showing a consistent phase and amplitude. Hence, no significant energy dependence could be detected.

Like accretion-powered, coherent pulsations from this source, the burst oscillation has an asymmetric profile, pointing to substantial harmonic content. Indeed, if we decompose the waveform into harmonic components, we find

a fundamental amplitude of 5.9% rms and a second harmonic amplitude of 3.4% rms. These amplitudes are well in excess of the amplitudes measured contemporaneously from the coherent pulsations (Figure 7, bottom panel). Furthermore, the burst oscillation appears to lag behind the coherent pulsation by about 0.07 cycles. We note, however, that the phase of the coherent pulsation shows a much larger scatter over the course of the outburst (Sanna et al. 2022), so we interpret the burst oscillation as being in phase alignment with the coherent pulsation, at least within the statistical uncertainty.

4 DISCUSSION

In this paper we reported an analysis of 7 Type-I X-ray bursts observed by *NICER* during the 2021 outburst of the AMXP Swift J1749. From time-resolved spectroscopy we found enhanced N_{H} values during the X-ray bursts compared with those found in the persistent emission prior to each burst. We detected a burst oscillation signal during the peak of the first burst entirely consistent with the known spin frequency of the neutron star (517.92 Hz). Additionally, we found that each X-ray burst occurs on top of an elevated persistent count rate. Time-resolved spectroscopy of the pre-burst emission showed that the black body parameters evolve to hotter temperatures closer to the onset of the X-ray burst. In this section we discuss each of these findings.

4.1 Type-I X-ray Bursts

4.1.1 X-ray Burst Spectral Characteristics

We find that all X-ray bursts from Swift J1749 for which we performed time-resolved spectroscopy exhibit typical spectral phenomenology (an increase in black body temperature during the burst rise, and steady decrease in the decay). This did, however, require all the fits to be performed while allowing N_{H} to vary. Marino et al. (2022) also found that allowing N_{H} to vary during spectral analysis of the full 2021 outburst of Swift J1749 improves the spectral fits. However, Marino et al. (2022) does not report values as large as those obtained from our burst fitting. We find that, during the X-ray bursts, the average N_{H} values were significantly higher than those found in the fits of the persistent emission. We interpret this raised N_{H} during the bursts as being a consequence of irradiation of the accretion disc by the X-ray burst emission. This interaction would cause the disc to “puff up” during the X-ray burst, thus increasing the line-of-sight absorption, as illustrated in Figure 8. This interpretation is strengthened by the fact that we would only be able to observe this increased line-of-sight absorption if the system is high-inclination, as Swift J1749 is ($i \approx 74^\circ - 77^\circ$; Altamirano et al. 2011). If our interpretation is correct, this would explain why these results have not, to our knowledge, been found in the time-resolved spectroscopy of other Type-I X-ray bursts (in low-inclination systems).

Allowing N_{H} to vary during the time-resolved spectroscopy of X-ray bursts has not, to our knowledge, been used to analyse X-ray bursts from eclipsing systems (there are 8 known eclipsing X-ray bursters out of a total of 85

bursting sources; Galloway et al. 2020). However, the varying N_{H} method has been performed before on superbursts by Ballantyne & Strohmayer (2004) and Keek et al. (2014)⁶. Both studies found that N_{H} increases by an order of magnitude during the superburst compared with the persistent emission, and follows a clear evolution. Ballantyne & Strohmayer (2004) explain the phenomenon with an increase in the scale height of the accretion disc, while Keek et al. (2014) suggest that disc wind driven by the superburst provides additional absorbing material. Whilst we see no clear evolution in N_{H} during the bursts themselves (likely due to poor statistics), the fact that we observe changes in N_{H} similar to those observed in much brighter superbursts is evidence that we might be seeing burst-disc interaction even during standard Type-I X-ray bursts.

There are arguments for certain orbital phases being associated with higher absorption, for example, due to the accretion stream over and under-flowing the accretion disc (see, e.g., Miškovičová et al. 2016). We checked to see if each burst was occurring at the same orbital phase, however the bursts all occurred at different points in the orbital phase.

We report the X-ray burst peak bolometric fluxes, fluences and τ values in Table 3 and will now compare them with the general population. In order to compare peak flux and fluence with Galloway et al. (2008), we calculated the normalised peak flux (defined as peak flux divided by Eddington flux) and normalised fluence (U_b , defined as fluence divided by Eddington flux), using Eddington flux found by Kuulkers et al. (2003). We find that the normalised peak flux values for B1 – 6, excluding B3, are all ~ 0.2 , placing them in the centre of the positively skewed Gaussian distribution of normalised peak fluxes for non-PRE bursts. B7 has a normalised peak flux of ~ 0.7 , placing it in the upper tail of the distribution. We find that all our analysed bursts have $U_b \approx 5$, placing them around the centre of the Gaussian distribution for non-PRE bursts. We also find that the values of τ for B1 – 6, excluding B3, are very high ($\sim 23 - 27$ s), placing them in the second peak in the bimodal distribution of non-PRE bursts. These values are in-line with what we expect due to the low peak fluxes of the bursts. For B7, which has a significantly higher peak flux than the other bursts, we find τ to be ~ 8 s, which is in the centre of the first peak of the bimodal distribution of the general population. These results are consistent with mixed H/He unstable burning (see, e.g., Galloway & Keek 2021) where the rp -process is dominant in B1 – 6, while B7 is more helium-rich.

4.1.2 Burst Oscillations

We have, for the first time, detected a burst oscillation in an X-ray burst of Swift J1749. The burst oscillation was found in the peak of B1 at a frequency of 517.92 Hz, which matches the known spin frequency of the neutron star (Sanna et al. 2022). Galloway et al. (2020) lists 16 sources which exhibit burst oscillations, three of which are persistent pulsars (see also Bilous & Watts 2019). Here we report on the fourth

⁶ Interestingly, both Ballantyne & Strohmayer (2004) and Keek et al. (2014) also find the Fe XXVI absorption line discussed in §3.3.2. We note that the sources discussed in both these papers are not high inclination (i.e. $i < 70^\circ$).

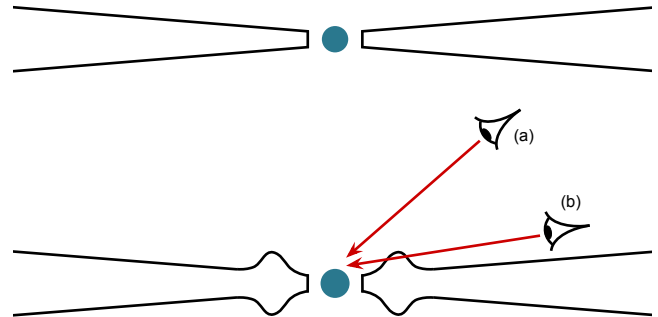


Figure 8. Schematic of neutron star and accretion disc, viewed edge-on. Top: a standard thin disc, bottom: a scenario where a Type-I X-ray burst has caused the inner accretion disc to “puff up”. We can see that this change in disc geometry will not affect line-of-sight absorption in a low-inclination system (a), but will in a high-inclination system (b).

persistent pulsar from which burst oscillations have been detected. These burst oscillations are typical with respect to fractional rms amplitude: the general population of burst oscillations have a median rms amplitude of 5% (Galloway et al. 2008; Ootes et al. 2017). We find burst oscillations in the peak of an X-ray burst, the burst phase in which 54% of oscillations are found (Galloway et al. 2008). However, only 25% of bursts with burst oscillations have $\tau > 10$ s, placing B1 in this minority ($\tau_{\text{B1}} = 30$ s). These results show that the burst oscillations we find in Swift J1749 are consistent with the general population.

4.2 Raised Pre-Burst Emission

We find that the persistent count rate slowly and systematically increases before the ignition of (almost) every X-ray burst we detected. This phenomenon has, to our knowledge, not been previously observed in other X-ray burst sources. From our spectral analysis, we find that the raised pre-burst emission is due to an increase in black body temperature of the thermal component in our model. Although we see that a thermal component is responsible, the statistical quality of the data did not allow us to resolve the spectrum into multiple thermal components representing disc emission and surface emission separately. Therefore, we cannot distinguish between disc and surface emission.

If we assume that the increase in pre-burst emission is due to thermal disc emission, this implies that the mass accretion rate (\dot{M}) through the disc rises in the ~ 200 s prior to the burst. One (unlikely) possibility is that the fluctuation in \dot{M} is not intrinsically related to the burst. Instead these fluctuations might be stochastic variations that happen throughout the outburst and are by chance aligned with some of our bursts. The fact that the pre-burst light curve profile in B7 varies from the previous bursts suggests that the variations are just stochastic. We investigated this idea by searching for random rises in persistent count rate *with-*

out the onset of an X-ray burst⁷. The elevated emission has a clearly discernible pattern in the light curve with a deviation of $\sim 8 \text{ cts s}^{-1}$. Inspecting the light curve of the whole outburst we found no instance of such a deviation other than the ones found immediately preceding the X-ray bursts. We therefore conclude that the raised pre-burst emission is connected to the burst ignition.

We must also ask why the count rate, and hence \dot{M} returns to normal after the X-ray burst occurred. A second possibility relating the raised pre-burst emission to the disc is that the X-ray burst itself acts as a feedback control on \dot{M} . From the time-resolved spectroscopy we found that N_{H} increases during the burst, which we argue is due to the disc puffing up in response to irradiation by the burst. This change in disc geometry will affect the rate of mass flow from the disc onto the neutron star surface that the disc can support, so we could speculate that it is the radiative impact on the disc that forces it back into its lower \dot{M} state.

The problem with this idea, however, is that there is no reason to believe that an increase in \dot{M} should always trigger an X-ray burst. The extra flux contributed during the raised pre-burst phase is only a very small fraction of the accretion fluence between bursts, so it is exceedingly unlikely that an X-ray burst would ignite every time precisely ~ 200 s after \dot{M} starts to increase. We therefore argue that the raised pre-burst emission is associated with the neutron star surface and not the accretion disc.

If we assume that the increase in pre-burst emission and rise in black body temperature is due to the stellar surface, we could attribute it to nuclear burning processes that lead into the unstable burst ignition. There are two phenomena discussed in the literature that are known to precede X-ray bursts: precursors and mHz quasi-periodic oscillations (mHz QPOs). “Precursors” are short, burst-like events lasting a few seconds which have been interpreted as being due to, for example, (i) deep layer or multi-layer burst ignition (Bhattacharyya & Strohmayer 2007), (ii) mechanisms related to multi-peaked bursts (Jonker et al. 2004), or (iii) shock-generated X-ray bursts before superbursts (Keek & Heger 2011; Keek 2012). These short events described as precursors are not similar to the pre-burst features we see from Swift J1749, which are over 200 s and seem to be due to changes in the persistent emission rather than additional features on top of the persistent emission. Therefore we can dismiss that the raised pre-burst emission we see in our bursts is related to the same phenomena.

The second phenomena seen preceding X-ray bursts are mHz QPOs. Revnivtsev et al. (2001) discovered a class of low-frequency (7–9 mHz), soft energy (1–5 keV) QPO with fractional rms amplitudes of $\approx 2\%$, which disappear after X-ray bursts. Heger et al. (2007) explained that these mHz QPOs could be caused by marginally stable nuclear burning on the neutron star’s surface, where the burning is only oscillatory close to the luminosity boundary between stable and unstable burning. Heger et al. (2007) also shows that

temperature fluctuations are possible in the burning layer during the oscillations. Altamirano et al. (2008) found that the triggering of a thermonuclear X-ray burst is also linked to the frequency of the QPO dropping below $\lesssim 9$ mHz. A possible interpretation of the pre-burst rises we see in our data is that these rises are the start of mHz QPOs that trigger an X-ray burst after just the rise of the first period. If we consider the “bump” before B7 to be half an oscillation, this gives us a possible QPO frequency of ~ 2 mHz, which is below the critical frequency found by Altamirano et al. (2008). We also find a fractional rms amplitude of $\sim 25\%$. Whilst mHz QPOs are similar to what we observe in Swift J1749, these values do not align with those established for typically seen mHz QPOs. Therefore we suggest that the raised pre-burst emission is related to mHz QPOs in that it is caused by a special case of marginally stable or confined burning process on the stellar surface that culminates in the unstable ignition of an X-ray burst.

If our interpretation is correct, and the raised pre-burst emission is due to a special marginally stable burning process, then we should also consider why this phenomenon is not routinely observed in other sources. We posit two possible explanations. Firstly, we note that mHz QPOs are quite rare (seen in only 6 sources; Mancuso et al. 2021, and references therein). Both observations and theory suggest that marginally stable burning only occur in a narrow range of luminosities ($L_{2-20 \text{ keV}} \approx 5 - 11 \times 10^{36} \text{ erg s}^{-1}$; Altamirano et al. 2008), a range which mHz QPO sources tend to only pass through during their outbursts. Swift J1749 stays within a narrow range of luminosities ($L_{2-20 \text{ keV}} \approx 1 - 2 \times 10^{36} \text{ erg s}^{-1}$) during its outburst. It is possible that this special marginally stable burning process occurs in this narrow range of luminosities that Swift J1749 happens to stay in during its outburst. Hence, specific neutron star and \dot{M} parameters may simply place Swift J1749 in a part of the marginally stable burning process regime that is not sampled by other X-ray burst sources. Secondly, as a pulsar, Swift J1749 has unusually high harmonic content (i.e., the overtone is often stronger than the fundamental), pointing to a rather unusual inner accretion geometry (Altamirano et al. 2011; Sanna et al. 2022). If we assume that other classical mHz QPO sources are indeed non-pulsating sources (and that the lack of observed pulsations is not due to rotational axis alignment with the magnetic axis), Swift J1749 would be the first mHz QPO source that is also an accreting millisecond pulsar and so has a stronger magnetic field than non-pulsating sources. Hence, we could speculate that we are observing a mHz QPO that is either magnetically confined to a local region of the stellar surface and/or distorted by the viewing angle (where the high inclination of the system may play a role).

ACKNOWLEDGEMENTS

A.A. thanks the referee for making helpful suggestions that improved the paper. A.A. also thanks M. & L. Albayati for their support. D.A. acknowledges support from the Royal Society. S.G. acknowledges the support of the CNES. T.G. has been supported in part by the Turkish Republic, Presidency of Strategy and Budget project, 2016K121370. G.C.M. was partially supported by PIP 0113 (CONICET)

⁷ This was found by taking the median and maximum deviation in each pointing, and taking the absolute difference between the two. We visually inspected pointings showing values higher than $\sim 4 \text{ cts s}^{-1}$. Other than in pointings containing either a burst or eclipse, there were no systematic deviations.

and received financial support from PICT-2017-2865 (AN-PCyT). A.M. is supported by the H2020 ERC Consolidator Grant “MAGNESIA” under grant agreement No. 817661 (PI: Rea) and National Spanish grant PGC2018-095512-BI00. A.M. is also partially supported by the program Unidad de Excelencia Maria de Maeztu CEX2020-001058-M, and by the PHAROS COST Action (No. CA16214).

DATA AVAILABILITY

This work made use of data provided by the High Energy Astrophysics Science Archive Research Center (HEASARC).

REFERENCES

- Albayati A. C., et al., 2021, *MNRAS*, **501**, 261
- Altamirano D., van der Klis M., Wijnands R., Cumming A., 2008, *ApJ*, **673**, L35
- Altamirano D., et al., 2010, *The Astronomer’s Telegram*, **2565**, 1
- Altamirano D., et al., 2011, *ApJ*, **727**, L18
- Arnaud K. A., 1996, in Jacoby G. H., Barnes J., eds, *Astronomical Society of the Pacific Conference Series Vol. 101, Astronomical Data Analysis Software and Systems V*. p. 17
- Ballantyne D. R., Strohmayer T. E., 2004, *ApJ*, **602**, L105
- Beardmore A. P., Godet O., Sakamoto T., 2006, *GRB Coordinates Network*, **5209**, 1
- Belloni T., Stella L., Bozzo E., Israel G., Campana S., 2010, *The Astronomer’s Telegram*, **2568**, 1
- Bhattacharyya S., Strohmayer T. E., 2007, *ApJ*, **656**, 414
- Bilou A. V., Watts A. L., 2019, *ApJS*, **245**, 19
- Bozzo E., Belloni T., Israel G., Stella L., 2010, *The Astronomer’s Telegram*, **2567**, 1
- Buccheri R., et al., 1983, *A&A*, **128**, 245
- Bult P., et al., 2019, *ApJ*, **885**, L1
- Bult P., et al., 2021a, *ApJ*, **907**, 79
- Bult P. M., et al., 2021b, *The Astronomer’s Telegram*, **14428**, 1
- Burrows D. N., et al., 2003, in *Proc. SPIE*. pp 1320–1325, doi:10.1117/12.461279
- Chenevez J., et al., 2010, *The Astronomer’s Telegram*, **2561**, 1
- Degenaar N., Koljonen K. I. I., Chakrabarty D., Kara E., Altamirano D., Miller J. M., Fabian A. C., 2016, *MNRAS*, **456**, 4256
- Degenaar N., et al., 2018, *Space Sci. Rev.*, **214**, 15
- Di Salvo T., Sanna A., 2022, in Bhattacharyya S., Papitto A., Bhattacharya D., eds, *Astrophysics and Space Science Library Vol. 465, Astrophysics and Space Science Library*. pp 87–124, doi:10.1007/978-3-030-85198-9_4
- Ferrigno C., et al., 2011, *A&A*, **525**, A48
- Folkner W. M., Williams J. G., Boggs D. H., Park R. S., Kuchynka P., 2014, *Interplanetary Network Progress Report*, **42-196**, 1
- Galloway D. K., Keek L., 2021, in Belloni T. M., Méndez M., Zhang C., eds, *Astrophysics and Space Science Library Vol. 461, Timing Neutron Stars: Pulsations, Oscillations and Explosions*. pp 209–262 (arXiv:1712.06227), doi:10.1007/978-3-662-62110-3_5
- Galloway D. K., et al., 2008, *ApJS*, **179**, 360
- Galloway D. K., et al., 2020, *ApJS*, **249**, 32
- Gehrels N., 2004, in *ESA Special Publication: 5th INTEGRAL Workshop on the INTEGRAL Universe*. p. 777
- HEASARC 2014, *HEASoft: Unified Release of FTOOLS and XANADU* (ascl:1408.004)
- Halpern J., 2006, *GRB Coordinates Network*, **5210**, 1
- Heger A., Cumming A., Woosley S. E., 2007, *ApJ*, **665**, 1311
- Jahoda K., et al., 2006, *ApJS*, **163**, 401
- Jonker P. G., Galloway D. K., McClintock J. E., Buxton M., Garcia M., Murray S., 2004, *MNRAS*, **354**, 666
- Jonker P. G., Torres M. A. P., Steeghs D., Chakrabarty D., 2013, *MNRAS*, **429**, 523
- Kaastra J. S., Bleeker J. A. M., 2016, *A&A*, **587**, A151
- Keek L., 2012, *ApJ*, **756**, 130
- Keek L., Heger A., 2011, *ApJ*, **743**, 189
- Keek L., Ballantyne D. R., Kuulkers E., Strohmayer T. E., 2014, *ApJ*, **789**, 121
- Krimm H. A., et al., 2013, *ApJS*, **209**, 14
- Kuulkers E., den Hartog P. R., in’t Zand J. J. M., Verbunt F. W. M., Harris W. E., Cocchi M., 2003, *A&A*, **399**, 663
- Lewin W. H. G., van Paradijs J., Taam R. E., 1993, *Space Sci. Rev.*, **62**, 223
- Lund N., et al., 2003, *A&A*, **411**, L231
- Mancuso G. C., Altamirano D., Méndez M., Lyu M., Combi J. A., 2021, *MNRAS*, **502**, 1856
- Marino A., et al., 2022, *MNRAS*, **515**, 3838
- Markwardt C. B., Strohmayer T. E., 2010, *ApJ*, **717**, L149
- Mereminskiy I. A., Grebenev S. A., Lutovinov A. A., Krivonos R. A., Kuulkers E., 2021, *The Astronomer’s Telegram*, **14427**, 1
- Miškovičová I., et al., 2016, *A&A*, **590**, A114
- Ootes L. S., Watts A. L., Galloway D. K., Wijnands R., 2017, *ApJ*, **834**, 21
- Palmer D., et al., 2006, *GRB Coordinates Network*, **5208**, 1
- Patruno A., Watts A. L., 2021, *Astrophysics and Space Science Library*, **461**, 143
- Pavan L., et al., 2010, *The Astronomer’s Telegram*, **2548**, 1
- Ponti G., Muñoz-Darias T., Fender R. P., 2014, *MNRAS*, **444**, 1829
- Remillard R. A., et al., 2022, *AJ*, **163**, 130
- Revnivtsev M., Churazov E., Gilfanov M., Sunyaev R., 2001, *A&A*, **372**, 138
- Sanna A., et al., 2022, *MNRAS*, **514**, 4385
- Schady P., Beardmore A. P., Marshall F. E., Palmer D. M., Rol E., Sato G., 2006, *GRB Coordinates Network*, **5200**, 1
- Strohmayer T., Bildsten L., 2006, in , Vol. 39, *Compact stellar X-ray sources*. pp 113–156
- Strohmayer T. E., Markwardt C. B., 2010, *The Astronomer’s Telegram*, **2569**, 1
- Strüder L., et al., 2001, *A&A*, **365**, L18
- Tauris T. M., van den Heuvel E. P. J., 2006, *Formation and evolution of compact stellar X-ray sources*. Cambridge University Press, Cambridge, pp 623–665
- Verner D. A., Ferland G. J., Korista K. T., Yakovlev D. G., 1996, *ApJ*, **465**, 487
- Wijnands R., Rol E., Cackett E., Starling R. L. C., Remillard R. A., 2009, *MNRAS*, **393**, 126
- Wilms J., Allen A., McCray R., 2000, *ApJ*, **542**, 914
- Worpel H., Galloway D. K., Price D. J., 2013, *ApJ*, **772**, 94
- Worpel H., Galloway D. K., Price D. J., 2015, *ApJ*, **801**, 60

APPENDIX A: VARYING N_{H} METHOD IN X-RAY BURST TIME-RESOLVED SPECTROSCOPY

In this appendix, we expand upon our investigations for the X-ray burst time-resolved spectroscopy presented in Section 3.2.3. We found that a single black body model,

$$\text{tbabs} \times (\text{bbodyrad} + \text{powerlaw})$$

with N_{H} and powerlaw components fixed to the best fit parameters from the persistent emission fits (see Table 2) resulted in large residuals. However, allowing N_{H} to vary freely reduced these residuals. In Figure A1 we show an example spectrum taken from the peak bin of B4. We can see the

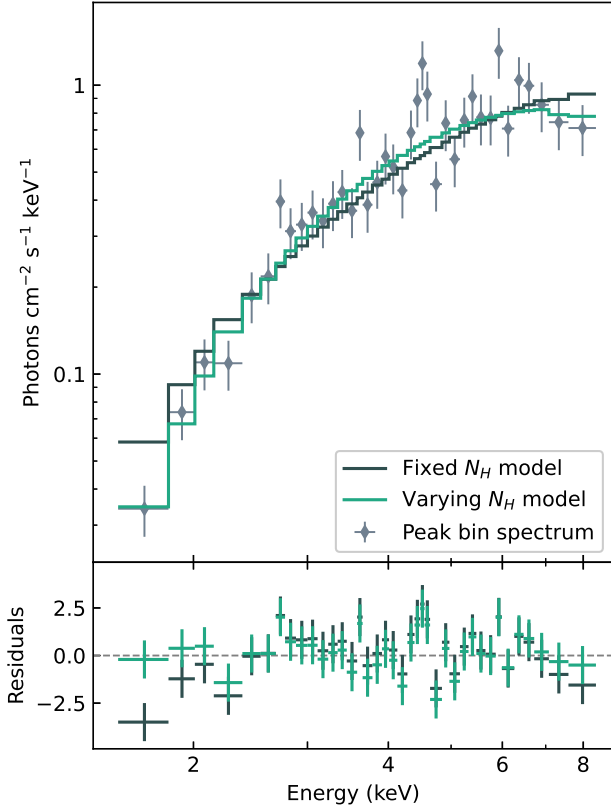


Figure A1. Burst 4 spectrum, models, and residuals from the peak of the burst (bin 4 of the time-resolved spectroscopy). Top: unfolded burst spectrum (`eufspec` command in `Xspec`), and best fit models for the fixed N_H method and varying N_H method. Bottom: residuals from each of the models (`delchi` command in `Xspec`).

model best fits for both the fixed and varying N_H methods, and the residuals. Figure A2 shows the residuals from the first 10 bins of B4, which covers 29s since the burst start time. The difference in residuals between the two models shows that the varying N_H model better fits the data, particularly in the lower and higher energy ranges of the spectra.

Reduced χ^2 panels from implementing both the fixed and varying N_H methods in the time-resolved spectroscopy of all analysed bursts can be seen in Figure A3. In each case, the reduced χ^2 values indicate that the fixed N_H method did not produce suitable fits, and allowing N_H to vary improved the fits.

We note that implementing the f_a -method (Worpel et al. 2013, 2015) to scale the persistent emission only produced reasonable fits when f_a was allowed to be negative, which is not a physically motivated option.

This paper has been typeset from a $\text{\TeX}/\text{\LaTeX}$ file prepared by the author.

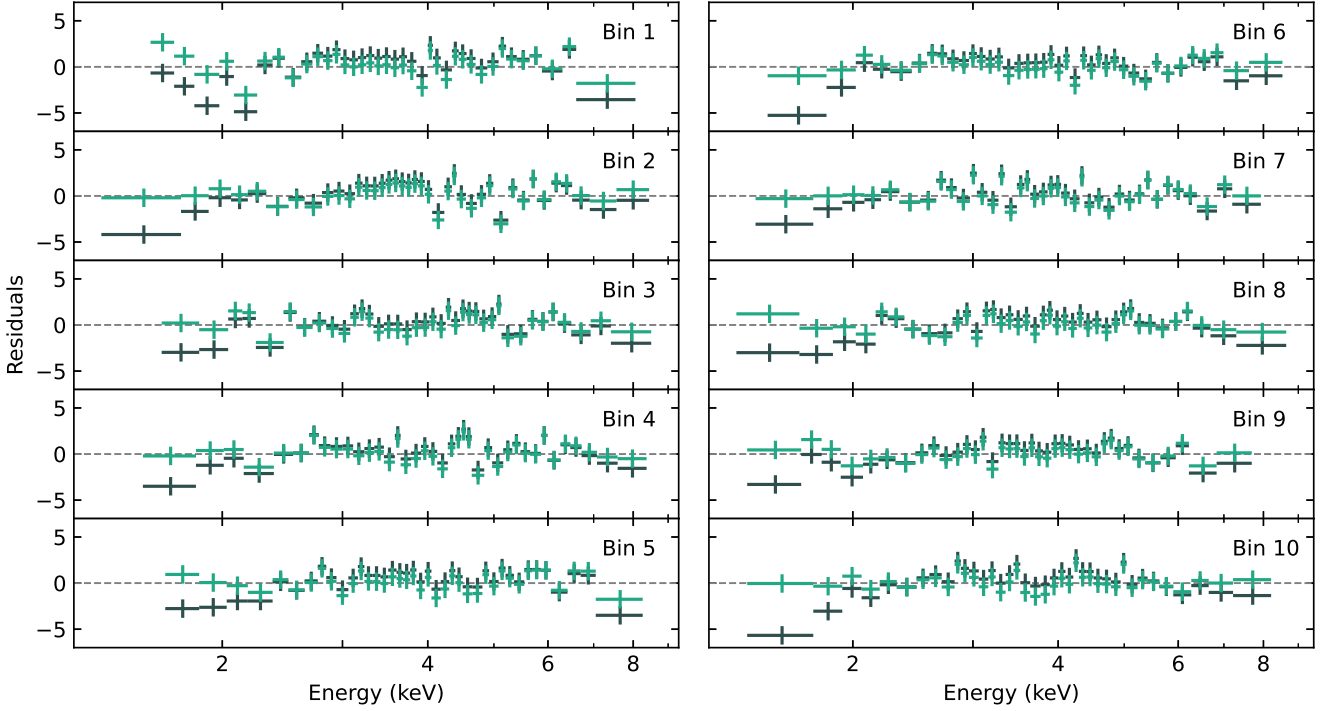


Figure A2. Residuals from the first 10 spectra used in the time-resolved spectroscopy of burst 4, where the spectra have been fitted with the fixed and varying N_{H} methods (`delchi` command in `Xspec`). The colour coding is as presented in Figure A1 (dark grey for fixed N_{H} method and teal for varying N_{H} method).

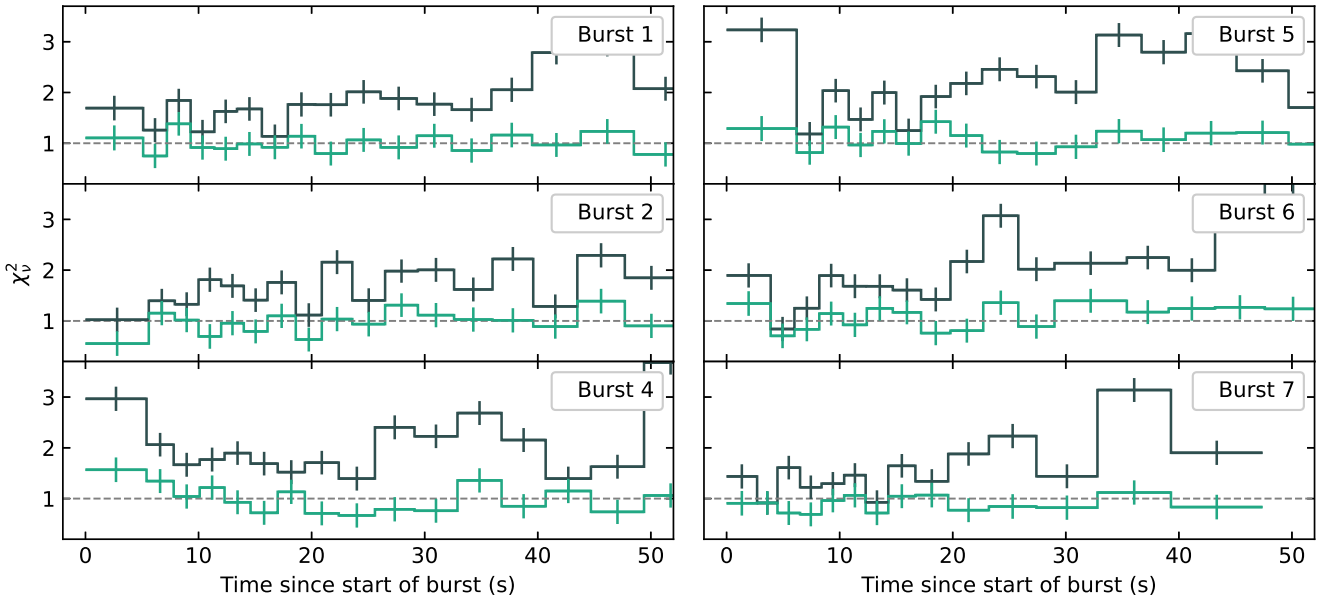


Figure A3. Reduced χ^2 panels from the time-resolved spectroscopy of each burst, where the spectra have been fitted using the fixed and varying N_{H} methods. The colour coding is as presented in Figure A1 (dark grey for fixed N_{H} method and teal for varying N_{H} method).